Statistical Image Reconstruction of Two Simultaneously Excited fMRI Slices

Daniel B. Rowe[1,2], Andrew S. Nencka[2]
[1]Department of Mathematics, Statistics and Computer Science, Marquette University
[2]Department of Biophysics, Medical College of Wisconsin

Abstract

In functional MRI, each slice in a volume is traditionally excited individually, measuring enough data in a single k-space array to reconstruct an image for that slice. However, simultaneously exciting multiple slices that make up a volume can produce sufficient data in a single k-space array to represent multiple slices. This single array of k-space data can be reconstructed into a single image representing the aliased slices, and then separated into individual images for each slice. A statistical description of an image representing two aliased slices using a single channel coil is presented. Image separation, utilizing calibration reference scans of each slice, through both an existing magnitude-only approach and a new complex-valued approach are described, and the statistical properties of these two image separation approaches are presented. Through examining the expected mean image and covariance matrix of the separated images, it is theoretically shown that correlations remain between images of slices through both approaches. Since the image separation process is not the inverse of the image aliasing process, the separated images have different statistical properties than slices excited individually. Through both theoretical and experimental data, the complex-valued approach is shown to out-perform the magnitude-only approach.

Key Words: fMRI, SENSE, image reconstruction, MRI, magnetic resonance imaging

1. Introduction

Since the advent of functional magnetic resonance imaging (fMRI), researchers have invested great efforts and have made significant progress on accelerating the acquisition of images of the slices needed to build up a single image volume. With the inception of parallel imaging (1), methods such as SENSE (2) and GRAPPA (3) have greatly contributed to the in-plane acceleration of images using multicoil arrays to reconstruct the image of a single slice. More recently, interest has been gaining momentum for the simultaneous excitation and acquisition of multiple parallel images of slices to build up a single volume. One justification for the simultaneous acquisition of images of slices is that they are temporally aligned, allowing for more accurate inferences to be made between them. The acquisition of images of two simultaneously excited slices in two experiments with a single channel coil has been presented (4, 5) and extended to multiple slices using multiple channel coils in a single experiment (6,7,8,9,10,11). The magnitude-only approach to two encoded slices using a single channel quadrature coil was presented using images from Cartesian echo-planar sampling (8,12) and presented using images from spiral echo-planar sampling (13). Here we describe both the previously presented magnitude-only image separation approach and a new complex-valued approach for separating two aliased images of two slices using a single channel quadrature coil experiment. The recent line of research utilizing complex-valued images and magnitude-phase time series models to compute fMRI activation (14,15,16) provides the motivation to separate complex-valued images over magnitude-only images.

The outline of this manuscript is as follows: The Methods section describes the image aliasing model and the two separation approaches. The Theory section describes the statistical properties of the separated images including their expected mean, variance, and correlation structure. The Results section presents results from both models on Monte

Carlo computer simulated and MRI machine experimental data. Finally, the Discussion and Conclusion section discusses the presented methods, findings, and comments on image separation.

2. Methods

Traditionally in fMRI, each slice that makes up a volume is excited individually, and enough data for that slice is measured in a single *k*-space array to reconstruct an image. However, it is possible to simultaneously excite two slices, measuring sufficient data in a single *k*-space array to be reconstructed into a single aliased image representing the two slices, and then separated into two images for the two slices.

2.1 Two Image Aliasing

Each measured voxel value in the aliased image is described as the sum of the two true voxel values from aliased slices *a* and *b* plus measurement noise

$$(y_R + iy_I) = (\rho_a \cos\theta_a + i\rho_a \sin\theta_a) + (\rho_b \cos\theta_b + i\rho_b \sin\theta_b) + (\varepsilon_R + i\varepsilon_I),$$

where y_R and y_I are the real and imaginary parts of the aliased voxel's measured value, ρ_a and θ_a are the true noiseless magnitude and phase for slice *a*, ρ_b and θ_b are the true noiseless magnitude and phase for slice *b*, while ε_R and ε_I are additive error for the real and imaginary parts of the aliased voxel's measured value. The process of aliasing two slices with a single coil can be equivalently represented for a given voxel as

$$\begin{pmatrix} y_R \\ y_I \end{pmatrix} = \begin{pmatrix} 1 & 0 & 1 & 0 \\ 0 & 1 & 0 & 1 \end{pmatrix} \begin{pmatrix} \rho_a \cos\theta_a \\ \rho_a \sin\theta_a \\ \rho_b \cos\theta_b \\ \rho_b \sin\theta_b \end{pmatrix} + \begin{pmatrix} \varepsilon_R \\ \varepsilon_I \end{pmatrix} \quad [1]$$

or $y=X_A\beta+\varepsilon$, where y is 2×1 vector representing the observed real and imaginary aliased image voxel values, X_A is 2×4 matrix describing the aliasing process, $\beta=(\rho_a\cos\theta_a,\rho_a\sin\theta_a,\rho_b\cos\theta_b,\rho_b\sin\theta_b)'$ is a 4×1 vector representing the voxel values for the two true fully acquired images, and ε is a 2×1 vector representing measurement error. In Eq. [1] we will assume that $E(\varepsilon_R,\varepsilon_I)'=0$ and $\text{cov}(\varepsilon_R,\varepsilon_I)'=\sigma^2 I_2$. The goal is to separate the images of the two slices in a manner such as $\hat{\beta} = X_A^{-1} y$. However, the aliasing matrix in Eq. [1], X_A, represents a system of two equations with four unknowns, as it is not square or invertible, and thus a unique solution to these equations for β cannot generally be found. One solution, proposed in (8,11), is to use the singular value decomposition (SVD) to calculate the Moore-Penrose pseudoinverse (17), which provides a unique solution in the least squares sense, but not necessarily the correct solution. We will examine the statistical properties of the previously proposed magnitude-only approach and our newly proposed complex-valued approach in the Theory section along with their performance in the Results section.

2.2 Calibration Reference Images

In order to perform the separation of two simultaneously excited slices, full field-of-view calibration "reference images" of the two slices need to be acquired. In a given fully acquired voxel, the measured reference images at time *t* are described as

$$\begin{pmatrix} y_{Rat} \\ y_{Iat} \\ y_{Rbt} \\ y_{Ibt} \end{pmatrix} = \begin{pmatrix} S_a \cos\phi_a \\ S_a \sin\phi_a \\ S_b \cos\phi_b \\ S_b \sin\phi_b \end{pmatrix} + \begin{pmatrix} n_{Rat} \\ n_{Iat} \\ n_{Rbt} \\ n_{Ibt} \end{pmatrix}, \quad [2]$$

for t=1,…,m, where y_{Rat} and y_{Iat} are the measured real and imaginary parts for the voxel in slice a, y_{Rbt} and y_{Ibt} are the measured real and imaginary parts for the voxel in slice b, S_a and ϕ_a are the true magnitude and phase of the voxel in slice a, S_b and ϕ_b are the true magnitude and phase of the voxel in slice b, while n_{Rat} and n_{Iat} are the real and imaginary parts of the measurement error for the voxel in slice a, n_{Rbt} and n_{Ibt} are the real and imaginary parts of the measurement error for the voxel in slice b, with m being the number of reference images. In Eq. [2] we will assume that $E(n_{Rat},n_{Iat},n_{Rbt},n_{Ibt})'=0$ and $\text{cov}(n_{Rat},n_{Iat},n_{Rbt},n_{Ibt})'=\sigma^2 I_4$. From these reference images, we calculate the averages $(\overline{y}_{Ra},\overline{y}_{Ia},\overline{y}_{Rb},\overline{y}_{Ib})'$, which are converted to magnitude and phase $(\overline{r}_a,\overline{\phi}_a,\overline{r}_b,\overline{\phi}_b)'$ to be used in separating the slices.

2.3 Magnitude-Only Image Separation

The motivation behind a magnitude-only separation of slice images, proposed in (8,11,12,18), is a reduction in the number of parameters to solve for. Eq. [1] can be equivalently written as

$$\begin{pmatrix} y_R \\ y_I \end{pmatrix} = \begin{pmatrix} \cos\theta_a & \cos\theta_b \\ \sin\theta_a & \sin\theta_b \end{pmatrix} \begin{pmatrix} \rho_a \\ \rho_b \end{pmatrix} + \begin{pmatrix} \varepsilon_R \\ \varepsilon_I \end{pmatrix} \qquad [3]$$

or $y=X_M\rho+\varepsilon$, where X_M is a 2×2 matrix representing the aliasing process, $\rho=(\rho_a,\rho_b)'$ is a 2×1 vector representing the voxel magnitude values for the two true fully acquired images, while y and ε are 2×1 vectors of measured values and measurement error respectively, as previously described. Now we can separate magnitude-only images of the two slices using the model in Eq. [3] by $\tilde{\rho}=X_M^{-1}y$, or for a given voxel,

$$\begin{pmatrix} \tilde{\rho}_a \\ \tilde{\rho}_b \end{pmatrix} = \frac{1}{\sin\overline{\Delta}} \begin{pmatrix} -\sin\overline{\phi}_b & \cos\overline{\phi}_b \\ \sin\overline{\phi}_a & -\cos\overline{\phi}_a \end{pmatrix} \begin{pmatrix} y_R \\ y_I \end{pmatrix}, \qquad [4]$$

where $\overline{\phi}_a$ and $\overline{\phi}_b$ are the phase of the average of the reference images, provided $\overline{\Delta}=\overline{\phi}_a-\overline{\phi}_b$ is not an integer multiple of π. In the Results section we will see that many voxels have differences in reference image phase close to zero.

2.4 Complex-Valued Image Separation

Instead of transforming Eq. [1] to Eq. [3] and separating via Eq. [4] with an estimate of the phase from the reference images, we can add two additional linear constraints in each voxel to Eq. [1] in order to obtain four equations and four unknowns as

$$\begin{pmatrix} y_R \\ y_I \\ v_R \\ v_I \end{pmatrix} = \begin{pmatrix} 1 & 0 & 1 & 0 \\ 0 & 1 & 0 & 1 \\ c_{11} & c_{12} & c_{13} & c_{14} \\ c_{21} & c_{22} & c_{23} & c_{24} \end{pmatrix} \begin{pmatrix} \rho_a\cos\theta_a \\ \rho_a\sin\theta_a \\ \rho_b\cos\theta_b \\ \rho_b\sin\theta_b \end{pmatrix} + \begin{pmatrix} \varepsilon_R \\ \varepsilon_I \\ \eta_R \\ \eta_I \end{pmatrix} \qquad [5]$$

or $y_C=X_C\beta+e$, where $y_C=(y_R,y_I,v_R,v_I)'$ is a 4×1 vector representing the "observed" aliased image values with additional constraint values $v=(v_R,v_I)'$, $X_C=[X_A;C]$ is a 4×4 matrix representing the voxel's reference image values with additional linear constraints, $\beta=(\rho_a\cos\theta_a,\rho_a\sin\theta_a,\rho_b\cos\theta_b,\rho_b\sin\theta_b)'$ is a 4×1 vector representing the values for the two true fully acquired images of the slices, and $e=(\varepsilon_R,\varepsilon_I,\eta_R,\eta_I)'$ is 4×1 vector representing measurement error $\varepsilon=(\varepsilon_R,\varepsilon_I)'$ along with constraint information $\eta=(\eta_R,\eta_I)'$. Here ";"

indicates a separation between rows in the matrix. With suitable selection of the constraint values c_{jk}, X_C is of full rank and we can separate the complex-valued images of the two slices using the model in Eq. [4] by $\hat{\beta} = X_C^{-1} y_C$. It should also be noted that separation using $\hat{\beta} = X_C^{-1} y_C$ and the least squares estimate $\hat{\beta} = (X_C' X_C)^{-1} X_C y_C$ are equivalent because X_C is square and invertible. It should also be noted that the least squares estimator for the fully acquired voxels can be written as $\hat{\beta} = (X_A' X_A + C'C)^{-1} (X_A', C')(y', v')'$, where $C'C$ acts as a regularizer for a matrix inverse.

One such set of constraints that can be used is that the imaginary parts of the true images are zero via $v=\eta=(0,0)'$ and C=[0,1,0,0;0,0,0,1]. Carrying out the separation process by matrix inverse, the separated voxel values for the two image slices are

$$\begin{pmatrix} \tilde{\rho}_a \cos\tilde{\theta}_a \\ \tilde{\rho}_a \sin\tilde{\theta}_a \\ \tilde{\rho}_b \cos\tilde{\theta}_b \\ \tilde{\rho}_b \sin\tilde{\theta}_b \end{pmatrix} = \frac{1}{\sin\overline{\Delta}} \begin{pmatrix} -\sin\overline{\phi}_b & \cos\overline{\phi}_b & -\cos\overline{\Delta} & -1 \\ 0 & 0 & \sin\overline{\Delta} & 0 \\ \sin\overline{\phi}_a & -\cos\overline{\phi}_a & 1 & \cos\overline{\Delta} \\ 0 & 0 & 0 & \sin\overline{\Delta} \end{pmatrix} \begin{pmatrix} y_R \\ y_I \\ 0 \\ 0 \end{pmatrix} \qquad [6]$$

where $\overline{\phi}_a$ and $\overline{\phi}_b$ are the phase of the average of the reference images, provided $\overline{\Delta} = \overline{\phi}_a - \overline{\phi}_b$ is not an integer multiple of π. Upon comparing Eq. [6] to Eq. [4], one can see that the separated real parts of the two images in Eq. [6] are identical to the separated magnitudes in Eq. [4] and the separated imaginary parts of the two images in Eq. [6] are zero. Thus, the magnitude-only separation approach can be explained as the addition of two linear constraints in order to obtain a unique matrix inverse separation.

Since the aliasing process is predicated on the measured image being comprised of the true values for the two slices plus measurement error, we can utilize the reference images and describe another constrained image reconstruction. Assuming that the true images for the two slices are similar to the reference images, we can add two linear constraints as C=[1,0-1,0;01,0,-1] and additional "observed" data $\nu_R = \overline{y}_{Ra} - \overline{y}_{Rb}$ and $\nu_I = \overline{y}_{Ia} - \overline{y}_{Ib}$, with $\eta=(0,0)'$. Carrying out the complex-valued image separation process by $\hat{\beta} = X_C^{-1} y_C$, because X_C is of full rank with orthogonal rows, the voxel values for the two separated images are

$$\begin{pmatrix} \hat{\rho}_a \cos\hat{\theta}_a \\ \hat{\rho}_a \sin\hat{\theta}_a \\ \hat{\rho}_b \cos\hat{\theta}_b \\ \hat{\rho}_b \sin\hat{\theta}_b \end{pmatrix} = \frac{1}{2} \begin{pmatrix} 1 & 0 & 1 & 0 \\ 0 & 1 & 0 & 1 \\ 1 & 0 & -1 & 0 \\ 0 & 1 & 0 & -1 \end{pmatrix} \begin{pmatrix} y_R \\ y_I \\ \nu_R \\ \nu_I \end{pmatrix}. \qquad [7]$$

In principle other linear constraints, or nonlinear constraints that can be approximated by linear constraints, can be utilized such as C=[1,-1-1,1;1,1,-1,-1] which again yields an X_C of full rank with orthogonal rows.

3. Theory

Since the image separation process is not the inverse of the image aliasing process, we need to examine the statistical properties of the separated images, such as expected means, variances, and correlations relative to the true values.

3.1 Magnitude-Only Image Separation

To examine the statistical properties of the magnitude-only image separation process, the expectation of Eq. [4], $E(\tilde{\rho}) = X_M^{-1} E(y)$, can be taken to yield

$$\mu_{MO} = E\begin{pmatrix} \tilde{\rho}_a \\ \tilde{\rho}_b \end{pmatrix} = \frac{1}{\sin(\overline{\phi}_a - \overline{\phi}_b)} \begin{pmatrix} \sin(\theta_a - \overline{\phi}_b) & \sin(\theta_b - \overline{\phi}_b) \\ \sin(\overline{\phi}_a - \theta_a) & \sin(\overline{\phi}_a - \theta_b) \end{pmatrix} \begin{pmatrix} \rho_a \\ \rho_b \end{pmatrix} \quad [8]$$

Similarly, the covariance matrix of the magnitude estimators, $\mathrm{cov}(\tilde{\rho}) = X_M^{-1} \mathrm{cov}(y)(X_M^{-1})'$, can be pursued. It can be shown that the expected covariance between the magnitude-only separated magnitudes is

$$\Sigma_{MO} = \mathrm{cov}\begin{pmatrix} \tilde{\rho}_a \\ \tilde{\rho}_b \end{pmatrix} = \frac{\sigma^2}{\sin^2(\overline{\phi}_a - \overline{\phi}_b)} \begin{pmatrix} 1 & -\cos(\overline{\phi}_a - \overline{\phi}_b) \\ -\cos(\overline{\phi}_a - \overline{\phi}_b) & 1 \end{pmatrix} \quad [9]$$

with their correlation being $-\cos(\overline{\phi}_a - \overline{\phi}_b)$. One can see that the magnitude-only separation process has challenges when $\overline{\phi}_a - \overline{\phi}_b$ is a multiple of π, does not contain signal from the other slice when $\overline{\phi}_a = \theta_a$ and $\overline{\phi}_b = \theta_b$, and the correlation between the separated magnitudes is zero when $\overline{\phi}_a - \overline{\phi}_b = \pi / 2$.

3.2 Complex-Valued Image Separation

To examine the statistical properties of the complex-valued image separation process, the expectation of the estimator in Eq. [7] can be determined. The expectation of the estimator for the voxels is $E(\hat{\beta}) = X_C^{-1} E(y_C)$, and is found to be

$$\mu_{CV} = E\begin{pmatrix} \hat{\rho}_a \cos\hat{\theta}_a \\ \hat{\rho}_a \sin\hat{\theta}_a \\ \hat{\rho}_b \cos\hat{\theta}_b \\ \hat{\rho}_b \sin\hat{\theta}_b \end{pmatrix} = \begin{pmatrix} \frac{1}{2}(\rho_a \cos\theta_a + S_a \cos\phi_a) & + & \frac{1}{2}(\rho_b \cos\theta_b - S_b \cos\phi_b) \\ \frac{1}{2}(\rho_a \sin\theta_a + S_a \sin\phi_a) & + & \frac{1}{2}(\rho_b \sin\theta_b - S_b \sin\phi_b) \\ \frac{1}{2}(\rho_b \cos\theta_b + S_b \cos\phi_b) & + & \frac{1}{2}(\rho_a \cos\theta_a - S_a \cos\phi_a) \\ \frac{1}{2}(\rho_b \sin\theta_b + S_b \sin\phi_b) & + & \frac{1}{2}(\rho_a \sin\theta_a - S_a \sin\phi_a) \end{pmatrix}. \quad [10]$$

In a similar fashion, the covariance matrix for the separated voxels is $\mathrm{cov}(\hat{\beta}) = X_C^{-1}$ $\mathrm{cov}(y_C)$ $(X_C^{-1})'$, and is found to be

$$\Sigma_{CV} = \mathrm{cov}\begin{pmatrix} \hat{\rho}_a \cos\hat{\theta}_a \\ \hat{\rho}_a \sin\hat{\theta}_a \\ \hat{\rho}_b \cos\hat{\theta}_b \\ \hat{\rho}_b \sin\hat{\theta}_b \end{pmatrix} = \frac{\sigma^2}{4} \begin{pmatrix} 1 & 0 & 1 & 0 \\ 0 & 1 & 0 & 1 \\ 0 & 1 & 1 & 0 \\ 1 & 0 & 0 & 1 \end{pmatrix} \quad [11]$$

where $\mathrm{cov}((v_R, v_I)') = 0$ because the reference images do not vary over the course of the experiment.

It has been noted that the magnitude is not a linear operator and that the magnitude-square correlation is asymptotically equivalent to the magnitude correlation (19,20). The expected mean magnitude-square is

$$\mu_{MS} = \begin{pmatrix} tr(\Sigma_{11}) + \mu_1'\mu_1 \\ tr(\Sigma_{22}) + \mu_2'\mu_2 \end{pmatrix}, \quad [12]$$

and the expected magnitude-square correlation between the separated complex-valued images is

$$\Lambda_{MS} = \begin{pmatrix} 2tr(\Sigma_{11}\Sigma_{11}') + 4\mu_1'\Sigma_{11}\mu_1 & 2tr(\Sigma_{12}\Sigma_{12}') + 4\mu_1'\Sigma_{12}\mu_2 \\ 2tr(\Sigma_{12}\Sigma_{12}') + 4\mu_1'\Sigma_{12}\mu_2 & 2tr(\Sigma_{22}\Sigma_{22}') + 4\mu_2'\Sigma_{22}\mu_2 \end{pmatrix} \quad [13]$$

where the elements of Eqs. [12] and [13] originate from μ_{CV}=[μ_1; μ_2], and $\sum_{CV}$=[$\sum_{11}$,$\sum_{12}$;$\sum_{21}$,$\sum_{22}$]. It can be shown when S_a=ρ_a, ϕ_a =θ_a and S_b=ρ_b, ϕ_b =θ_b that the expected correlation between the magnitude squares is

$$cor_{MS} = \left(\frac{1 + 4\rho_a\rho_b \cos(\theta_a - \theta_b)}{[(1 + 4\rho_a^2)(1 + 4\rho_b^2)]^{1/2}} \right),$$

which is very small when $\theta_a - \theta_b$ =π/2.

It should be noted that if one were to use the reference image values in a local neighborhood of ℓ voxels, then 2ℓ additional rows will be added to y_C in Eq. [5] corresponding to the ν's for these voxels, then $S_a\cos\phi_a$ in Eq. [10] becomes $\sum S_{aj}\cos\phi_{aj}$ and $S_b\cos\phi_b$ becomes $\sum S_{bj}\sin\phi_{bj}$ where j=1,…,(ℓ+1) indexes voxel number in the neighborhood, including the central one.

4. Results

To assist in illustrating the separation methodology in the Methods and Theory sections, two experimentally acquired echo planar imaging time series data sets, with matching fMRI acquisition parameters, of a spherical Agar phantom will be utilized. Both data sets were acquired on a GE Discovery MR750 MRI scanner (General Electric, Milwaukee, WI). For both data sets, a Cartesian gradient-recalled echo planar imaging sequence is employed. The first data set consists of 10 fully acquired slices while the second consists of 5 slices with aliasing between slices 1 and 6, slices 2 and 7, slices 3 and 8, slices 4 and 9, and slices 5 and 10. Both data sets consist of 720 volume images that were acquired with a repetition time (TR) of 1 s, an echo time (TE) of 42.5 ms, a band width (BW) of 166 kHz, a field-of-view (FOV) of 24 cm, slice thickness (SLTH) of 4.0 mm, a flip angle (FA) of 45 degrees, and an effective echo spacing (EESP) of 752 μs for a 96×96 *k*-space acquisition and reconstructed matrix. The fully acquired and aliased *k*-space arrays were Nyquist ghost corrected by the amount calculated from navigator echoes (21) then inverse Fourier transform reconstructed. The first aliased slice along with the first and sixth fully acquired reference slices were selected for analysis. The first 5 aliased images and fully acquired pairs of reference images were discarded from analysis to ensure steady state magnetization. The subsequent m=2 fully acquired reference images are averaged and used to separate the n=715 volumes of aliased images.

To correct for drift in the gradients, and any difference in baseline phase between the reference images and the aliased images, a phase correction was performed on the aliased images (18). In the phase correction, a mask was created from the average complex

reference images for voxels that exceeded 10% of its maximum magnitude. After applying the mask, the phase φ_{SR} of the (sum of the reference) images was subtracted from the original aliased phase φ_{OAt} of each of the n (original aliased) images in the time series by dividing each image by the normalized sum. The phase φ_{AV} of the average of the n (original aliased minus sum of reference phase) images was then subtracted by computing their average and dividing each image by its normalized version. A plane was then fit to the phase φ_{OAt}-φ_{SR}-φ_{AV} of each of the n masked (original aliased minus sum of reference and average phase) images for each of the non-overlapping and overlapping object regions. The fitted phase φ_{PFt} for each unmasked image was then subtracted by dividing each unmasked image by a complex number with this fitted phase and unit magnitude. The phase φ_{SR} of the sum of the reference images was finally added back to each of the n unmasked (original aliased minus sum of reference, average, and plane fitted phase) images to yield the n adjusted φ_{OAt}-φ_{AV}-φ_{PFt} aliased images. To correct for a difference in magnitude between the fully acquired and aliased images, the magnitude of the sum of the reference images was divided by the magnitude of the sum of the aliased images, averaged over the union of the masked regions for the two slices, then the aliased images were multiplied by this factor. The scaling factor for the acquired and simulated aliased data were 1.2922 and 1.0007, respectively. The corrected phase with scaled aliased magnitudes is separated using the previously described methods.

4.1 Average of Fully Acquired Complex-Valued Images plus Complex-Valued Random Noise

To illustrate the slice separation methods under known theoretical conditions, the first two volumes of the data set of fully acquired complex-valued images were averaged and used for true fully acquired reference images. To obtain true aliased images, pairs of slice images (slice 1 with 6, etc.) were added. Fully acquired reference images were obtained by adding independent and identically distributed noise with a variance as given in Fig. 4c to the real and imaginary parts of slice a and variance, as given in Fig. 4d, to the real and imaginary parts to slice b. Aliased images were obtained by adding independent and identically distributed noise to the real and imaginary parts, as calculated from the experimental aliased images of the second set of data. For the simulated data, m=2 volumes of n_z=10 fully acquired 96×96 reference images were generated along with 720 volumes of n_z/2=5 aliased images with the first five removed to result in n=715 volumes. The first aliased slice, where slices a=1 and b=6 are aliased, was selected for separation with the a=1 and b=6 fully acquired slices.

Figure 1 contains magnitudes and phases of reference, aliased, and separated images. In Fig.1a and Fig. 1b are the magnitude and phase of the reference image for slice a, while in Fig. 1c and Fig. 1d are the magnitude and phase of the reference image for slice b. Note that there is some minimal Nyquist ghosting in the reference images that is particularly evident in the phase. The ratio of the magnitudes of the reference images for slices a and b is presented in Fig. 1e while the difference in phase between reference images of slice a and b is in Fig. 1f. The difference in reference image phase is particularly relevant in the denominator of the magnitude-only image separation used in Eq. [4]. To illustrate the slice separation methods, both their application to a single image and the expected values of their application are calculated.

The magnitude and phase of the first aliased image from Eq. [1] are shown in Fig. 1g and 1h respectively. Note that the magnitude of the aliased image appears visually similar to

the sum of the magnitude images in Figs. 1a and 1c. For the magnitude-only image separation approach, the expected magnitudes using from Eq. [8] are displayed in Fig. 1i for slice *a* and Fig. 1j for slice *b*, with the separated magnitudes for the first image in the series from Eq. [4] in Fig. 1k for slice *a* and Fig. 1l for slice *b*. Note that both the expected magnitudes in Figs. 1m and 1n from Eq. [8] in addition to the separated magnitudes in Figs. 1k and 1l using the magnitude-only approach from Eq. [4] have some challenges when the difference in phase of the reference images shown in Fig. 1f is clos e to zero. Some of the magnitudes using the magnitude-only separation approach are negative, thus illustrating the challenges with the magnitude-only approach.

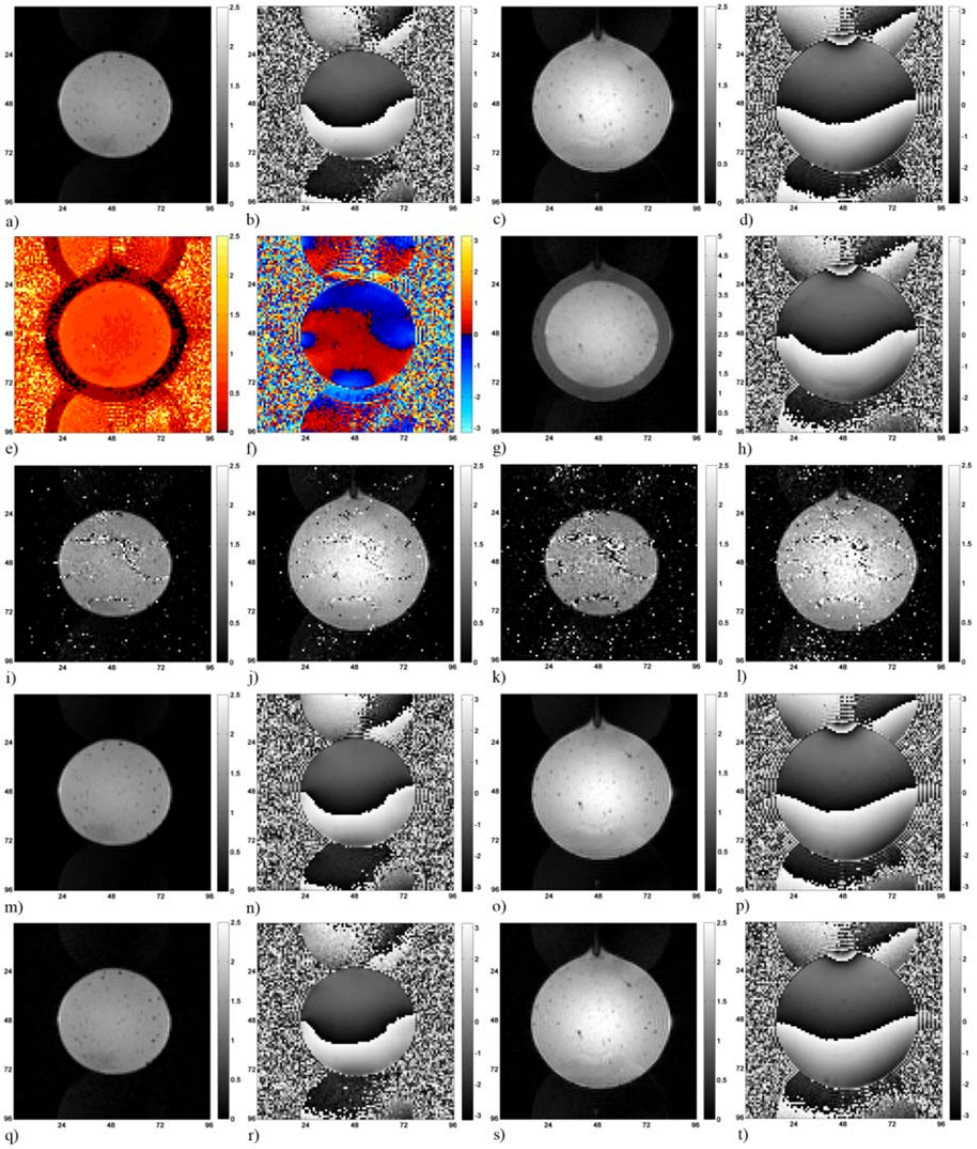

Figure 1: Images for simulated data. Reference images magnitude (a) and phase (b) for slice *a*, magnitude (c) and phase (d) for slice *b*, the ratio of magnitudes (e), the difference of phases (f) between slices *a* and *b*, with the aliased image magnitude (g) and phase (h). Magnitude-only expected image magnitude for slice *a* (i) and for slice *b* (j), with magnitude-only separated image magnitude for slice *a* (k) and for slice *b* (l). Complex-valued expected image magnitude (m) and phase (n) for slice *a*, magnitude (o) and phase (p) for slice *b*, with complex-valued separated image magnitude (q) and phase (r) for slice *a*, and magnitude (s) and phase (t) for slice *b*.

Derived from Eq. [10], the complex-valued expected image magnitude and phase for slice *a* are displayed in Fig. 1m and 1n respectively, while the complex-valued expected image magnitude and phase for slice *b* are displayed in Fig. 1o and 1p respectively. Using Eq. [7] on the first aliased image in the series in Fig. 1g and Fig. 1h, the complex-valued separated image magnitude and phase for slice *a* are displayed in Fig. 1q and 1r respectively, while the complex-valued separated image magnitude and phase for slice *b* are displayed in Fig. 1s and 1t. Note that the separated image using the complex-valued approach are visually very similar to the expected values and reference images, thus the complex-valued approach performs extremely well in separating the slices in addition to not being dependent upon the difference in phase of the reference images.

Figure 2 contains variances and correlations of the separated images. In Figs. 2a and 2b are the separated image variances for slices *a* and *b* respectively using the magnitude-only approach. In Fig. 2c and 2d are the separated image variances for slices *a* and *b* respectively using the complex-valued approach. The expected image variances from Eq. [9] and [11] and the separated image variances were visually nearly identical and thus the expected variances are not shown. Note that the variances using the complex-valued approach are smaller than the variances using the magnitude-only approach.

The correlations presented about the center voxel in slices *a* and *b* in Figs. 2e through 2t correspond to the magnitude-only and complex-valued approaches. The expected image correlations from Eqs. [9], [11], and [13] are not presented because all their values are zero except for a select few that contain a single one or minus one. The separated image correlation shown in Fig. 2e is for slice *a* magnitude and slice *a* magnitude, shown in Fig. 2f is for slice *a* magnitude and slice *b* magnitude, and shown in Fig. 2g is for slice *b* magnitude and slice *b* magnitude. Note that there is a distinct near -1 correlation between a voxels' separated magnitude in slice *a* and the separated magnitude in slice *b* and almost no correlation with other voxels.

The correlations presented about the center voxel in slices *a* and *b* in Fig. 2h through 2t correspond to the complex-valued approach. The separated image correlation shown in Fig. 2h is for slice *a* real and slice *a* real, shown in Fig. 2i is for slice *a* real and slice *a* imaginary, shown in Fig. 2j is for slice *a* real and slice *b* real, shown in Fig. 2k is for slice *a* real and slice *b* imaginary, shown in Fig. 2l is slice *a* imaginary and slice *a* imaginary, in Fig. 2m is for slice *a* imaginary and slice *b* real, shown in Fig. 2n is for slice *a* imaginary and slice *b* imaginary, shown in Fig. 2o is for slice *b* real and slice *b* real, shown in Fig. 2p is for slice *b* real and slice *b* imaginary, and shown in Fig. 2q is for slice *b* imaginary and slice *b* imaginary. The correlations between the real and imaginary parts of the images separated using the complex-valued approach appear similar to their expected values which are not shown, namely that there is a correlation of 1 in a voxel with its same complex component and almost no correlation with other voxels.

From the separated images using the complex-valued approach, the magnitudes were computed and their correlations are presented in Figs. 2r through Fig. 2t. The expected magnitude-square correlations are asymptotically equivalent to magnitude correlations using the complex-valued approach but are not presented as they are all zero except for a single value that is the correlation of a voxel in slice *a* with the same voxel in slice *b*. The correlation for slice *a* magnitude and slice *a* magnitude is in Fig. 2r, for slice *a* magnitude and slice *b* magnitude is in Fig. 2s, for slice *b* magnitude and slice *b* magnitude is in Fig. 2t. The separated image correlations for both the magnitude-only and complex-valued approaches are similar to the expected image correlations with the exception that low dark red and blue separated correlations are absent in the expected correlations.

To further examine the slice separation methods under simulated experimental conditions, the first data set of 720 fully acquired complex-valued images were artificially aliased by summing pairs of slice images (slices 1 and 6, etc.) with the first five removed to result in n=715 volumes. The first m=2 fully acquired reference images were averaged and used for separation. The first aliased slice was selected for separation

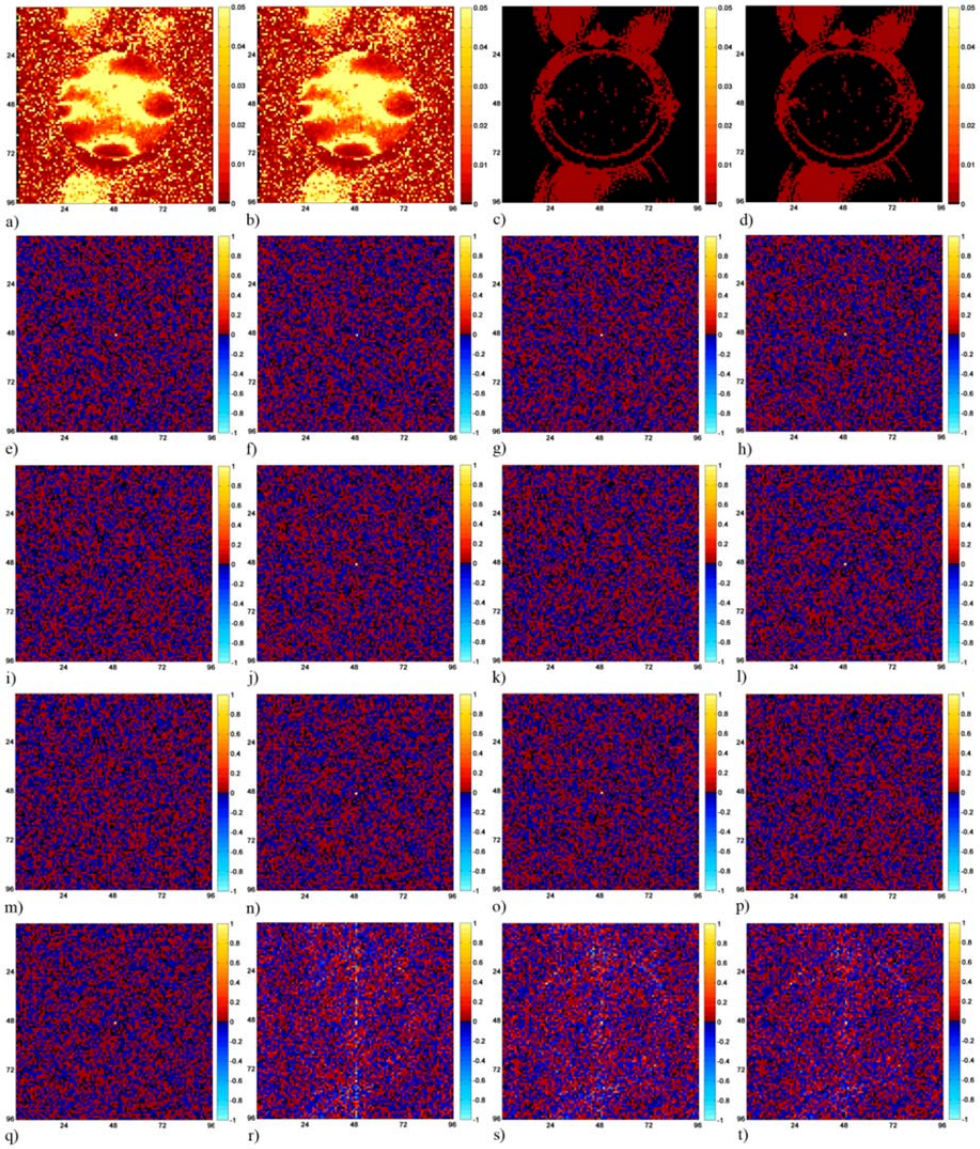

Figure 2: Variances and correlations for simulated data. Magnitude-only separated image variance for slice *a* (a) and for slice *b* (b), with complex-valued separated image variance for slice *a* (c) and for slice *b* (d). Magnitude-only separated image correlation for magnitudes of slices *a* and *a* (e), slices *a* and *b* (f), and slices *b* and *b* (g). Complex-valued separated image correlation for slice *a* real and slice *a* real (h), for slice *a* real and slice *a* imaginary (i), for slice *a* real and slice *b* real (j), for slice *a* real and slice *b* imaginary (k), for slice *a* imaginary and slice *a* real (l), for slice *a* imaginary and slice *b* real (m), for slice *a* imaginary and slice *b* imaginary (n), for slice *b* real and slice *b* real (o), for slice *b* real and slice *b* imaginary (p), for slice *b* imaginary and slice *b* imaginary (q), for slice *a* magnitude and slice *a* magnitude (r), for slice *a* magnitude and slice *b* magnitude (s), for slice *b* magnitude and slice *b* magnitude (t).

with the first and sixth fully acquired slices. The separated images are not shown here, as they are visually very similar to those in the next example of acquired aliased images.

4.2 Experimental Aliased Complex-Valued Images

To finally illustrate the slice separation methods under actual experimental conditions, the second data set of 720 aliased complex-valued with the first five removed to result in n=715 volumes were used. The first m=2 fully acquired reference images were averaged and used for separation. The first aliased slice was selected for separation with the a=1st and b=6th fully acquired slices.

Figure 3 contains magnitudes and phases of reference and separated images. In Fig.3a and 3b are the magnitude and phase of the reference image for slice *a*, while in Fig. 3c and 3d are the magnitude and phase of the reference image for slice *b*. Note that there is some minimal Nyquist ghosting in the reference images that is particularly evident in the phase. The ratio of the magnitudes of the reference images for slices *a* and *b* is presented in Fig. 3e while the difference in phase between reference images of slice *a* and *b* is in Fig. 3f. The difference in reference image phase is particularly relevant in the denominator of the magnitude-only image separation in Eq. [4]. To illustrate the slice separation methods, their application to a single image and the average of their application to all images are presented.

The magnitude and phase of the first aliased image are in Fig. 3g and 3h respectively. Note that the magnitude of the aliased image appears visually similar to the sum of the magnitude images in Fig. 3a and 3c. For the magnitude-only approach, the magnitudes of the average of the images are displayed in Fig. 3i and 3j for slices *a* and *b* respectively, while the separated magnitudes for the first image in Fig. 3g and Fig. 3h are in Fig. 3k and 3l for slices *a* and *b* respectively. Note that just as in the simulation example, the separated magnitudes in Figs. 3k and 3l from the magnitude-only approach in Eq. [4] have some challenges when the difference in phase of the reference images in Fig. 3f is close to zero. Some of the magnitudes using the magnitude-only approach are negative, thus highlighting the challenges with the magnitude-only approach.

Derived from Eq. [7], the magnitude and phase of the average image using the complex-valued separation approach for slice *a* are displayed in Fig. 3m and 3n respectively, while the magnitude and phase of the average image for slice *b* are displayed in Fig. 3o and 3p. Derived using the complex-valued separation approach in Eq. [7], the magnitude and phase of the first image in the series for slice *a* are displayed in Fig 3q and 3r respectively, while the magnitude and phase of the first image for slice *b* are displayed in Fig. 3s and 3t. Note that the separated images using the complex-valued approach are visually very similar to the average values and the reference images, thus it performs extremely well in separating the slices in addition to not being dependent upon the difference in phase of the reference images.

Figure 4 contains variances and correlations of the separated images. In Fig. 4a and 4b are the separated image variances for slices *a* and *b* respectively using the magnitude-only approach, In Fig. 4c and 4d are the separated image variances for slices *a* and *b* respectively using the complex-valued approach. Note that the image variances for the magnitude-only approach are significantly larger than those for the complex-valued approach, and that there is a similarity between the separated image variances and the simulated and expected image variances in the previous example.

The correlations presented about the center voxel in slices *a* and *b* in Fig. 4e through 4t correspond to the magnitude-only and complex-valued approaches. The separated image correlation shown in Fig. 4e is for slice *a* magnitude and slice *a* magnitude, shown in Fig. 4f is for slice *a* magnitude and slice *b* magnitude, and shown in Fig. 4g is for slice *b* magnitude and slice *b* magnitude. Note that there is a distinct near -1 correlation between

a voxels' separated magnitude in slice *a* and the separated magnitude in slice *b* and almost no correlation with other voxels.

The correlations presented about the center voxel in slices *a* and *b* in Fig. 4h through 4t correspond to the complex-valued approach. The separated image correlation shown in Fig. 4h is for slice *a* real and slice *a* real, shown in Fig. 4i is for slice *a* real and slice *a* imaginary, shown in Fig. 4j is for slice *a* real and slice *b* real, shown in Fig. 4k is for slice *a* real and slice *b* imaginary, shown in Fig. 4l is for slice *a* imaginary and slice *a*

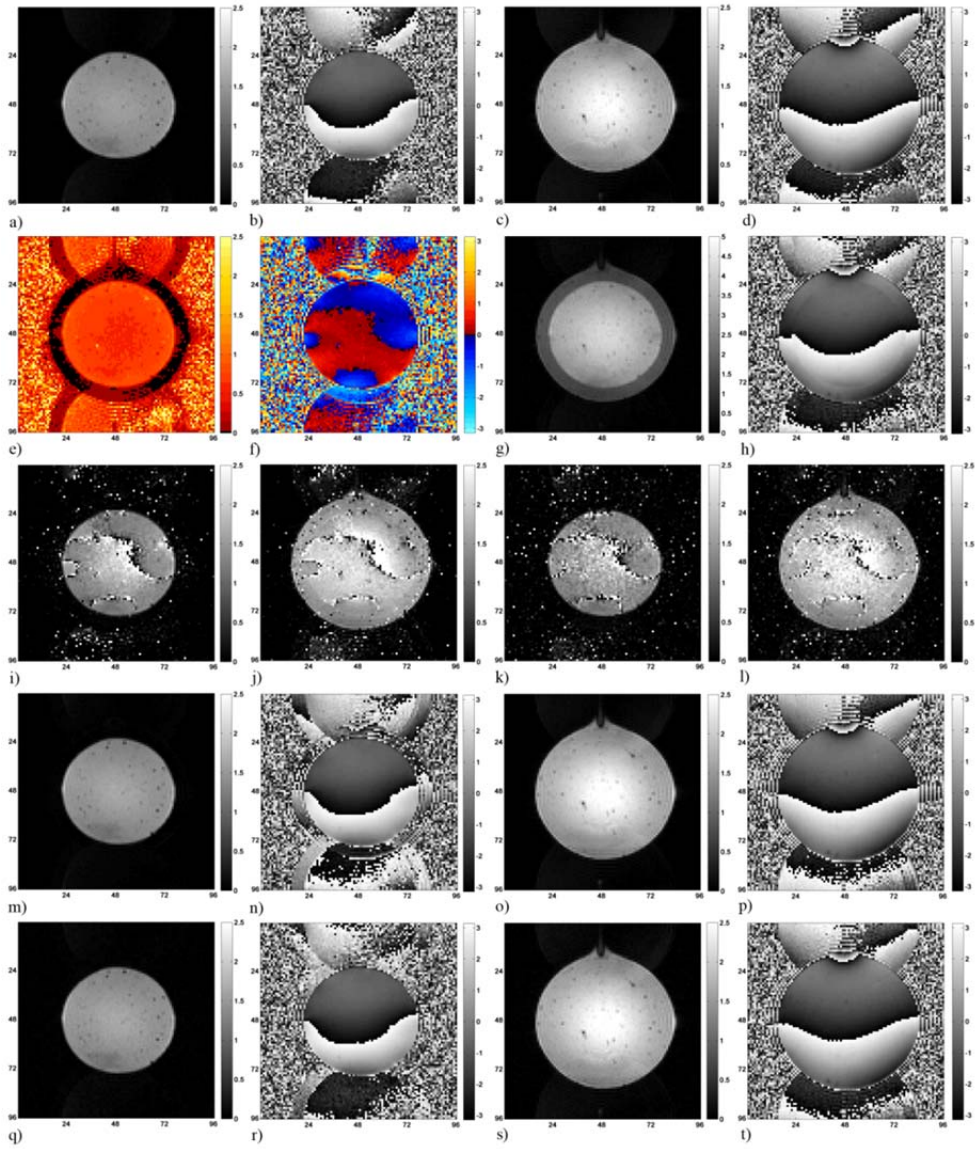

Figure 3: Images for experimental data. Reference images magnitude (a) and phase (b) for slice *a*, magnitude (c) and phase (d) for slice *b*, the ratio of magnitudes (e), the difference of phases (f) between slices *a* and *b*, with the aliased image magnitude (g) and phase (h). Magnitude-only average separated image magnitude for slice *a* (i) and for slice *b* (j), with magnitude-only separated image magnitude for slice *a* (k) and for slice *b* (l). Complex-valued magnitude (m) and phase (n) of average separated image for slice *a*, magnitude (o) and phase (p) of average separated image for slice *b*, with complex-valued separated image magnitude (q) and phase (r) for slice *a*, and magnitude (s) and phase (t) for slice *b*.

imaginary, shown in Fig. 4m is for slice *a* imaginary and slice *b* real, shown in Fig. 4n is for slice *a* imaginary and slice *b* imaginary, shown in Fig. 4o is for slice *b* real and slice *b* real, shown in Fig. 4p is for slice *b* real and slice *b* imaginary, while shown in Fig. 4q is for slice *b* imaginary and slice *b* imaginary. Note that the separated image correlations appear similar to their expected values in Fig. 2. The correlations between the real and imaginary parts of the images separated using the complex-valued approach appear

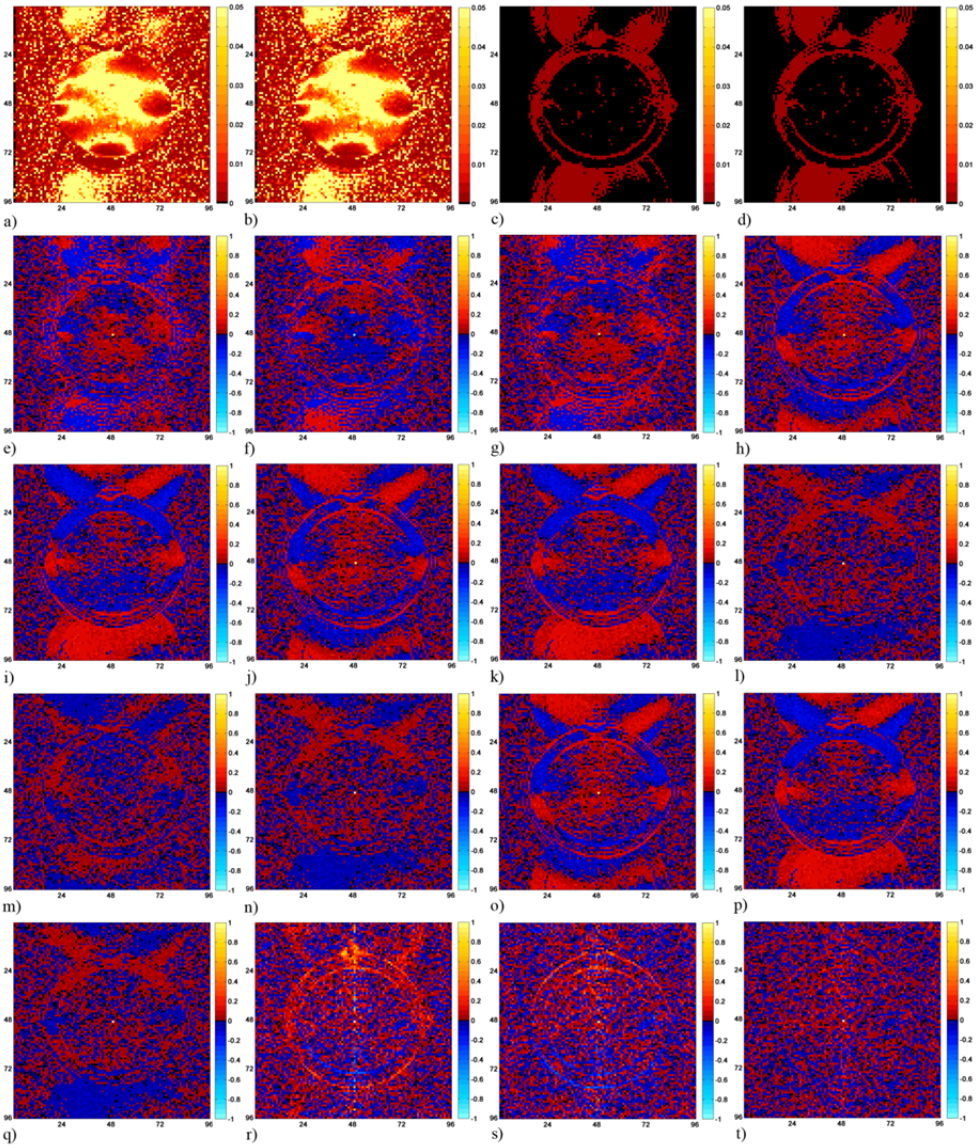

Figure 4: Variances and correlations for experimental data. Magnitude-only separated image variance for slice *a* (a) and for slice *b* (b), with complex-valued separated image variance for slice *a* (c) and for slice *b* (d). Magnitude-only separated image correlation for magnitudes of slices *a* and *a* (e), slices *a* and *b* (f), and slices *b* and *b* (g). Complex-valued separated image correlation for slice *a* real and slice *a* real (h), for slice *a* real and slice *a* imaginary (i), for slice *a* real and slice *b* real (j), for slice *a* real and slice *b* imaginary (k), for slice *a* imaginary and slice *a* real (l), for slice *a* imaginary and slice *b* real (m), for slice *a* imaginary and slice *b* imaginary (n), for slice *b* real and slice *b* real (o), for slice *b* real and slice *b* imaginary (p), for slice *b* imaginary and slice *b* imaginary (q), for slice *a* magnitude and slice *a* magnitude (r), for slice *a* magnitude and slice *b* magnitude (s), for slice *b* magnitude and slice *b* magnitude (t).

similar to their expected values, namely that there is a correlation of 1 in a voxel with its same complex component and almost no correlation with other voxels.

From the separated images using the complex-valued approach, the magnitudes were computed and their correlations are presented in Fig. 4r through Fig. 4t. The correlation for slice *a* magnitude and slice *a* magnitude is in Fig. 4r, for slice *a* magnitude and slice *b* magnitude is in Fig. 4s, for slice *b* magnitude and slice *b* magnitude is in Fig. 4t. The separated image correlations for both the magnitude-only approach and the complex-valued approach exhibit almost no correlation with other voxels except for very low correlation outlining the previously aliased slices attributed to a small difference between the phase of the sum of the reference images and the aliased images from phase due to gradient heating. Fitting a higher order polynomial would decrease this difference.

5. Discussion and Conclusions

In this manuscript, we have described the theory and application of both a previously derived magnitude-only approach and our newly defined complex-valued approach to separating aliased slices. It was highlighted that the magnitude-only approach has challenges separating the slices when the difference in phase between the reference images is close to a multiple of π and optimal when the difference is $\pi/2$. The experimental data and simulated data derived from the experimental data illustrate that such phase differences can be a challenge to control in long echo time, gradient recalled echo images with well displaced slices and an imperfect shim. From the theoretical statistical results, it is apparent that a voxels in a given slice can be correlated with the corresponding voxel in the other slice with the magnitude-only and complex-valued separation approaches. It was shown in the Results that the complex-valued approach performed better than the magnitude-only approach in terms of separated images.

New work in this manuscript separates the complex-valued images from two slices in a single aliased complex-valued image. Since the magnitude-only and complex-valued slice separation methods are performed in image space, *k*-space subsampling schemes such as partial *k*-space, SENSE, and GRAPPA can also be utilized to further increase the speed at which a single volume image is acquired. Analysis of complex-valued images in fMRI has been receiving increasing attention (14,15,16) and thus it is important to reconstruct complex-valued images. Future work on this topic includes extending to the aliasing of more than two slices, to more than one coil, combining with a statistical examination of SENSE (22), and application to experimental human and animal data.

References

1. Hyde JS, Jesmanowicz A, Froncisz W, Kneeland JB, Grist TM, Campagna NF Parallel image acquisition from noninteracting local coils. J Magn Reson 1986;70:512–517.

2. Pruessmann KP, Weiger M, Scheidegger MB, Boesiger P. SENSE: Sensitivity Encoding for Fast MRI. Magn Reson Med1999;42, 952–962.

3. Griswold MA, Jamob PM, Heidemann RM, Nikkka M, Jellus V, Wang J, Kiefer B, Haase A. Generalized autocalibrating partially parallel acquisition (GRAPPA). Magn Reson Med 2002; 47:1202-1210.

4. Muller S. Multifrequency selective RF pulses for multislice MR imaging. Magn Reson Med 1988;6:364–371.

5. Souza SP, Szumowski J, Dumoulin CL, Plewes DP, Glover G. SIMA: simultaneous multislice acquisition of MR images by Hadamard-encoded excitation. J Comput Assist Tomogr 1988;12:1026–1030.

6. Moeller S, Auerbach E, van de Moortele P-F, Adriany G, Ugurbil K. Functional MRI with 16-fold reduction using multibanded, multisite sampling. Proc Intl Soc Magn Reson Med 2008;16:2366.
7. Moeller S, Yacoub E, Auerbach E, Ohlman C, Ugurbil K. Unaliasing of multiband multislice EPI and GRE imaging with GRAPPA. Proc Intl Soc Magn Reson Med 2009;17:1544.
8. Jesmanowicz A, Li S-J, Hyde JS. Multi-slice two- and four-fold acceleration with single- and eight-channel coils, respectively. Proc Intl Soc Magn Reson Med 2009;17:1089.
9. Moeller S, Yacoub E, Olman CA, Auerbach E, Strupp J, Harel N, Ugurbil K. Multiband multislice GE-EPI at 7 Tesla, with 16-fold acceleration using partial parallel imaging with application to high spatial and temporal whole-brain fMRI. Magn Reson Med 2010;63:1144–1153.
10. Feinberg DA, Moeller S, Smith SM, Auerbach E, Ramanna S, Glasser MF, Miller KL, Ugurbil K, Yacoub E. Multiplexed echo planar imaging for sub-second whole brain fMRI and fast diffusion imaging. PLoS ONE 2010;5:e15710.
11. Jesmanowicz A, Nencka AS, Li S-J, Hyde JS. Two-Axis Acceleration of Functional Connectivity Magnetic Resonance Imaging by Parallel Excitation of Phase-Tagged Slices and Half k-Space Acceleration. Brain Connectivity 2011;1:81–90.
12. Shefchik, DS, Jesmanowicz, A, Budde, M, Nencka, AS. Single-coil two-fold accelerated spin-echo phase-SENSE imaging of the rodent brain at 9.4T. Proc Intl Soc Magn Reson Med 2012, 20:2229.
13. Islam H, Glover GH. Quadrature slice-encoding for reduced scan time. Proc. Intl Soc Magn Reson Med 2012, 20:2285.
14. Rowe DB, Logan BR. A complex way to compute fMRI activation. Neuroimage 2004;23:1078–92.
15. Rowe DB. Modeling both the magnitude and phase of complex-valued fMRI data. Neuroimage 2005;25(4):1310–24.
16. Arja SK, Feng Z, Chen Z, Caprihan A, Kiehl KA, Adali T, Calhoun VD. Changes in fMRI magnitude data and phase data observed in block-design and event-related tasks. Neuroimage 2010;49: 3149–3160.
17. Harville DA. Matrix Algebra From a Statistician's Perspective. Springer; 2008.
18. Jesmanowicz A, Nencka AS, Hyde JS. Two-Fold Phase Encoded SENSE Acceleration with a Single-Channel Coil. Proc Intl Soc Magn Reson Med 2011,19:2797.
19. Rowe DB, Nencka AS. Induced Correlation in FMRI Magnitude Data from k-Space Preprocessing Proc Intl Soc Mag Reson Med 2009; 17:1721.
20. Nencka AS, Hahn AD, Rowe DB. A Mathematical Model for Understanding Statistical Effects of *k*-space (AMMUST-k) Preprocessing on Observed Voxel Measurements in fcMRI and fMRI, J Neurosci Meth 2009;181, 268-282.
21. Nencka, AS, Hahn, AD, Rowe, DB. The use of Three Navigator Echoes in Cartesian EPI reconstruction Reduces Nyquist Ghosting. Proc Intl Soc Magn Reson Med 2008;16:3032.
22. Bruce IP, Karaman MM, Rowe DB. A Statistical Examination of SENSE Image Reconstruction via an Isomorphism Representation. Magn Reson Imaging 2011; 29:1267-1287.